Crystal Structure and the Paraelectric-to-Ferroelectric Phase Transition of Nanoscale BaTiO$_3$

Millicent B. Smith,[†] Katharine Page,[‡] Theo Siegrist,[§] Peter L. Redmond,[†]
Erich C. Walter,[†] Ram Seshadri,[‡] Louis E. Brus,[†] and Michael L. Steigerwald*,[†]

*Department of Chemistry, Columbia University, 3000 Broadway, New York, New York 10027,
Materials Department and Materials Research Laboratory, University of California,
Santa Barbara, California 93106, and Bell Laboratories, 600 Mountain Avenue,
Murray Hill, New Jersey 07974*

Received August 3, 2007; E-mail: mls2064@columbia.edu

Abstract: We have investigated the paraelectric-to-ferroelectric phase transition of various sizes of nanocrystalline barium titanate (BaTiO$_3$) by using temperature-dependent Raman spectroscopy and powder X-ray diffraction (XRD). Synchrotron X-ray scattering has been used to elucidate the room temperature structures of particles of different sizes by using both Rietveld refinement and pair distribution function (PDF) analysis. We observe the ferroelectric tetragonal phase even for the smallest particles at 26 nm. By using temperature-dependent Raman spectroscopy and XRD, we find that the phase transition is diffuse in temperature for the smaller particles, in contrast to the sharp transition that is found for the bulk sample. However, the actual transition temperature is almost unchanged. Rietveld and PDF analyses suggest increased distortions with decreasing particle size, albeit in conjunction with a tendency to a cubic average structure. These results suggest that although structural distortions are robust to changes in particle size, what is affected is the coherency of the distortions, which is decreased in the smaller particles.

Introduction

Barium titanate (BaTiO$_3$) is a ferroelectric oxide that undergoes a transition from a ferroelectric tetragonal phase to a paraelectric cubic phase upon heating above 130 °C. In cubic perovskite BaTiO$_3$, the structure of which is displayed in Figure 1a, titanium atoms are octahedrally coordinated by six oxygen atoms. Ferroelectricity in tetragonal BaTiO$_3$ is due to an average relative displacement along the *c*-axis of titanium from its centrosymmetric position in the unit cell and consequently the creation of a permanent electric dipole. The tetragonal unit cell is shown in Figure 1b. The elongation of the unit cell along the *c*-axis and consequently the deviation of the *c/a* ratio from unity are used as an indication of the presence of the ferroelectric phase.[1–3]

Ferroelectric properties and a high dielectric constant make BaTiO$_3$ useful in an array of applications such as multilayer ceramic capacitors,[4,5] gate dielectrics,[6] waveguide modulators,[7,8]
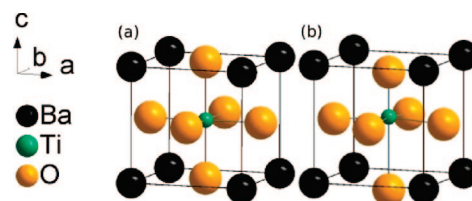
Figure 1. Unit cell of BaTiO$_3$ in both the (a) cubic *Pm*-3*m* structure and (b) tetragonal *P4mm* structure. In the tetragonal unit cell, atoms are displaced in the *z*-direction, and the cell is elongated along the *c*-axis. Atom positions: Ba at (0, 0, 0); Ti at (1/2, 1/2, *z*); O1 at (1/2, 1/2, *z*); and O2 at (1/2, 0, *z*). Displacements have been exaggerated for clarity.

IR detectors,[9] and holographic memory.[10] The dielectric and ferroelectric properties of BaTiO$_3$ are known to correlate with size, and the technological trend toward decreasing dimensions makes it of interest to examine this correlation when sizes are at the nanoscale.[11–16]

[†] Columbia University.
[‡] University of California.
[§] Bell Laboratories.

(1) Jaffe, B.; Cook, W. R.; Jaffe, H. *Piezoelectric Ceramics*, Vol. 3; Academic Press: New York, 1971.
(2) Lines, M. E.; Glass, A. M. *Principles and Applications of Ferroelectrics and Related Materials*; Clarendon Press: Oxford, 1977.
(3) Strukov, B. A.; Levanyuk, A. P. *Ferroelectric Phenomena in Crystals*; Springer-Verlag: Berlin, 1998.
(4) Wang, S. F.; Dayton, G. O. *J. Am. Ceram. Soc.* **1999**, *82*, 2677–2682.
(5) Hennings, D.; Klee, M.; Waser, R. *Adv. Mater.* **1991**, *3*, 334–340.
(6) Yildirim, F. A.; Ucurum, C.; Schliewe, R. R.; Bauhofer, W.; Meixner, R. M.; Goebel, H.; Krautschneider, W. *Appl. Phys. Lett.* **2007**, *90*, 083501/1–083501/3.
(7) Tang, P.; Towner, D. J.; Meier, A. L.; Wessels, B. W. *IEEE Photonic Tech. Lett.* **2004**, *16*, 1837–1839.

(8) Petraru, A.; Schubert, J.; Schmid, M.; Buchal, C. *Appl. Phys. Lett.* **2002**, *81*, 1375–1377.
(9) Pevtsov, E. P.; Elkin, E. G.; Pospelova, M. A. *Proc. SPIE−Int. Soc. Opt. Am.*, **1997**, *3200*, 179−182.
(10) Funakoshi, H.; Okamoto, A.; Sato, K. *J. Mod. Opt.* **2005**, *52*, 1511–1527.
(11) Shaw, T. M.; Trolier-McKinstry, S.; McIntyre, P. C. *Annu. Rev. Mater. Sci.* **2000**, *30*, 263–298.
(12) Frey, M. H.; Payne, D. A. *Phys. Rev. B* **1996**, *54*, 3158–3168.
(13) Zhao, Z.; Buscaglia, V.; Vivani, M.; Buscaglia, M. T.; Mitoseriu, L.; Testino, A.; Nygren, M.; Johnsson, M.; Nanni, P. *Phys. Rev. B* **2004**, *70*, 024107.
(14) Buscaglia, V.; Buscaglia, M. T.; Vivani, M.; Mitoseriu, L.; Nanni, P.; Terfiletti, V.; Piaggio, P.; Gregora, I.; Ostapchuk, T.; Pokorny, J.; Petzelt, J. *J. Eur. Ceram. Soc.* **2006**, *26*, 2889–2898.

Many experimental and theoretical[17–25] studies have indicated that the phase-transition temperature of $BaTiO_3$ is size-dependent, with the ferroelectric phase becoming unstable at room temperature when particle diameter decreases below a critical size. However, both theoretical and experimental reports of this critical size encompass a broad range of sizes. The experimental discrepancies may arise because of intrinsic differences between ferroelectric samples, because the transition is sensitive to conditions such as compositional variation,[26] lattice defects,[12] strain,[27] or surface charges.[20] Furthermore, the differences in cell parameters between the two phases are small compared to other sources of broadening in diffraction data, likely leading to an overestimation of the critical size. Recent work by Fong et al. on perovskite ($PbTiO_3$) thin films indicates that ferroelectric behavior persists down to a thickness of only three unit cells,[25] a value significantly less than that suggested by previous experimental studies.

Several theoretical studies have been particularly useful in furthering the understanding of the observed behavior of ferroelectrics at small sizes.[17] However, ferroelectrics are particularly sensitive to surface effects, making modeling increasingly complicated as dimensions are reduced. Many models based on Landau theory[18] overestimate critical sizes; it has been suggested that this overestimation has resulted from the use of material parameters in the free-energy expression that were derived from the bulk material.[19] Spanier et al. have found by theoretical modeling that certain surface termination of thin films can stabilize polarization down to a thickness of only several unit cells.[20] Their calculations, which take into account experimentally determined nanoscale material parameters, estimate the critical size for a $BaTiO_3$ sphere to be 4.2 nm. Other theoretical treatments, such as effective Hamiltonian and ab initio calculations, have predicted the presence of ferroelectricity in perovskite films as thin as three unit cells.[23,24]

Various experimental probes of the structure of $BaTiO_3$ have revealed a complex and sometimes controversial picture. In the study of bulk material, structural transformations have been explained by averaging domains that are locally rhombohedral.[28,29] For the tetragonal phase, the titanium atoms are distorted in the $\langle 111 \rangle$ directions and oriented with a net displacement in the *c*-direction. A number of studies have reported evidence of disorder within $BaTiO_3$ above the transition temperature, supporting the existence of distortions within the cubic phase.[30–32] X-ray diffraction (XRD) studies produce data that are consistent with an increasingly cubic structure at smaller particle sizes, not distinguishing between average and local structure.[12,33] In contrast, Raman results have supported the existence of tetragonal symmetry at small dimensions, even though it was not discernible by XRD.[34] The disagreement between Raman and diffraction studies suggests that the phase transition in bulk $BaTiO_3$ is complex, with order−disorder as well as displacive character.[12,35,36]

Extended X-ray absorption fine structure (EXAFS) and X-ray absorption near-edge structure (XANES) studies of bulk $BaTiO_3$ have supported a dominant order−disorder component to the structural phase transitions.[29] In EXAFS and XANES analysis of 10, 35, and 70 nm $BaTiO_3$ particles,[37] Frenkel et al. find titanium displacements for all samples studied, in contrast to their cubic macroscopic crystal structures from laboratory XRD. Petkov et al.[38] have recently demonstrated the use of the pair distribution function (PDF) to understand local structure distortions and polar behavior in $Ba_xSr_{1-x}TiO_3$ ($x = 1, 0.5, 0$) nanocrystals. They found that locally, refining over the first 15 Å, the tetragonal model was the best fit to the experimental PDF; however, over longer distances (15−28 Å), the cubic model was the best fit. Their conclusion was that 5 nm $BaTiO_3$ is on average cubic, but that tetragonal-type distortions in the Ti−O distances are present within the cubic structure. They did not, however, find the distortions to be inherent to small particles because they were not present in the perovskite $SrTiO_3$.

Several preparation strategies have been reported in recent years for high-quality, well-defined $BaTiO_3$ nanocrystalline samples. Hydrothermal or solvothermal methods have been systematically used to make nanocrystalline $BaTiO_3$.[39–42] O'Brien et al.[43] and Urban et al.[21,44] have produced $BaTiO_3$ particles and rods, respectively, from the reaction of a bimetallic alkoxide precursor with hydrogen peroxide. Niederberger et al. report a solvothermal preparation of 5 nm particles of $BaTiO_3$ and

(15) Hoshina, T.; Kakemoto, H.; Tsurumi, T.; Wada, S.; Yashima, M. *J. Appl. Phys.* **2006**, *99*, 054311–054318.

(16) Yashima, M.; Hoshina, T.; Ishimura, D.; Kobayashi, S.; Nakamura, W.; Tsurumi, T.; Wada, S. *J. Appl. Phys.* **2005**, *98*, 014313.

(17) Duan, W.; Liu, Z. -R. *Curr. Opin. Solid State Mater. Sci.* **2006**, *10*, 40–51.

(18) Wang, C. L.; Smith, S. R. P. *J. Phys.: Condens. Matter* **1995**, 7163–7171.

(19) Akdogan, E. K.; Safari, A. *J. Appl. Phys.* **2007**, *101*, 064114.

(20) Spanier, J. E.; Kolpak, A. M.; Urban, J. J.; Grinberg, I.; Ouyang, L.; Yun, W. S.; Rappe, A. M.; Park, H. *Nano Lett.* **2006**, *6*, 735–739.

(21) Urban, J. J.; Spanier, J. E.; Lian, O. Y.; Yun, W. S.; Park, H. *Adv. Mater.* **2003**, *15*, 423–426.

(22) Urban, J. J. Synthesis and Characterization of Transition Metal Oxide and Chalcogenide Nanostructures. Ph.D. Dissertation, Harvard University, Cambridge, MA, 2004.

(23) Ghosez, P.; Rabe, K. M. *Appl. Phys. Lett.* **2000**, *76*, 2767–2769.

(24) Meyer, B.; Vanderbilt, D. *Phys. Rev. B* **2001**, *63*, 205426.

(25) Fong, D. D.; Stephenson, G. B.; Streiffer, S. K.; Eastman, J. A.; Auciello, O.; Fuoss, P. H.; Thompson, C. *Science* **2004**, *304*, 1650–1653.

(26) Lee, S.; Liu, Z. -K.; Randall, C. A. *J. Appl. Phys.* **2007**, *101*, 054119.

(27) Choi, K. J.; Biegalski, M.; Li, Y. L.; Sharan, A.; Schubert, J.; Uecker, R.; Reiche, P.; Chen, Y. B.; Pan, X. Q.; Gopalan, V.; Chen, L. -Q.; Schlom, D. G.; Eom, C. B. *Science* **2004**, *306*, 1005–1009.

(28) Kwei, G. H.; Lawson, A. C.; Billinge, S. J. L.; Chong, S. -W. *J. Phys. Chem.* **1993**, *97*, 2368–2377.

(29) Ravel, B.; Stern, E. A.; Vedrinskii, R. I.; Kraizman, V. *Ferroelectrics* **1998**, *206–207*, 407–430.

(30) Zalar, B.; Laguta Valentin, V.; Blinc, R. *Phys. Rev. Lett.* **2003**, *90*, 037601.

(31) Lambert, M.; Comes, R. *Solid State Commun.* **1968**, *6*, 715–719.

(32) Comes, R.; Lambert, M.; Guinier, A. *Acta Crystallogr., Sect. A: Cryst. Phys., Diffr., Theor. Gen. Crystallogr.* **1970**, *26*, 244–254.

(33) Wada, S.; Tsurumi, T.; Chikamori, H.; Noma, T.; Suzuki, T. *J. Cryst. Growth* **2001**, *229*, 433–439.

(34) El Marssi, M.; Le Marrec, F.; Lukyanchuk, I. A.; Karkut, M. G. *J. Appl. Phys.* **2003**, *94*, 3307–3312.

(35) Wada, S.; Suzuki, T.; Osada, M.; Kakihana, M.; Noma, T. *Jpn. J. Appl. Phys.* **1998**, *37*, 5385–5393.

(36) Noma, T.; Wada, S.; Yano, M.; Suzuki, T. *Jpn. J. Appl. Phys.* **1996**, *80*, 5223–5233.

(37) Frenkel, A. I.; Frey, M. H.; Payne, D. A. *J. Synchrotron Radiat.* **1999**, *6*, 515–517.

(38) Petkov, V.; Gateshki, M.; Niederberger, M.; Ren, Y. *Chem. Mater.* **2006**, *18*, 814–821.

(39) Jung, Y.-J.; Lim, D. -Y.; Nho, J. -S.; Cho, S. -B.; Riman, R. E.; Lee, B. W. *J. Cryst. Growth* **2005**, *274*, 638–652.

(40) Yosenick, T.; Miller, D.; Kumar, R.; Nelson, J.; Randall, C.; Adair, J. *J. Mater. Res.* **2005**, *20*, 837–843.

(41) Guangneng, F.; Lixia, H.; Xueguang, H. *J. Cryst. Growth* **2005**, *279*, 489–493.

(42) Joshi, U. A.; Yoon, S.; Baik, S.; Lee, J. S. *J. Phys. Chem. B* **2006**, *110*, 12249–12256.

(43) O'Brien, S.; Brus, L.; Murray, C. B. *J. Am. Chem. Soc.* **2001**, *123*, 12085–12086.

(44) Urban, J. J.; Yun, W. S.; Gu, Q.; Park, H. *J. Am. Chem. Soc.* **2002**, *124*, 1186–1187.

Table 1. Particle Size Dependence on Solvent Composition

water: isopropanol (v:v)	particle size (nm)
1:0	70 ± 10
40:60	60 ± 10
30:70	45 ± 9
20:80	26 ± 5
0:1	~ 10

$SrTiO_3$ from titanium isopropoxide and metallic barium or strontium in benzyl alcohol.[45]

Here, we describe the use of a bimetallic alkoxide precursor in conjunction with solvothermal techniques to produce high-quality nanoparticles of $BaTiO_3$ with controllable sizes. We have studied particles with average sizes of 26, 45, and 70 nm by temperature-dependent Raman spectroscopy and XRD and with room temperature Rietveld and atomic PDF analysis of high-energy, high momentum-transfer synchrotron X-ray diffraction data. The sample particles are unstrained, because they are not thin-film samples and are compositionally homogeneous with, in particular, no discernible OH impurities that are known to plague many low-temperature solution preparations of ferro-electric oxides.[12,33,36]

The complementary structural methods we employ provide information on different time and length scales. Raman spectra reflect the local symmetry around the scattering sites and are averaged over different parts of the sample. The X-ray techniques both allow an average depiction of the structure (through pattern matching and Rietveld analysis) and provide information on the near-neighbor length scale through PDF.

The outcomes of the current study are consistent between the different techniques and are somewhat surprising. Raman spectroscopy indicates that the small particles undergo a more diffuse phase transition than in the bulk, although the T_C remains nearly unchanged. Careful temperature-dependent XRD studies show that all sizes of particles are tetragonal until close to the bulk T_C, and yet the smaller particles seem more cubic by using the c/a ratio as the metric. Average (Rietveld) and local (PDF) structure analyses of X-ray synchrotron data show that as the particle size is reduced, there is a clear and surprising trend toward increasing structural distortion. The increase in the off-centering of the titanium cation as particle size decreases in conjunction with the decrease in the c/a ratios is consistent with diminished structural coherence in smaller particles.

Experimental Section

Preparation of BaTiO₃ Nanoparticles. Anhydrous benzene, isopropanol, dendritic barium (99.99%), and titanium isopropoxide (99.999%) were obtained from Aldrich Chemical Co. and used as received. Sintered pieces of $BaTiO_3$ were also purchased from Aldrich for use as a bulk standard. The bimetallic precursor $BaTi[OC_3H_7]_6$ was prepared according to Urban et al.[44] Parr acid digestion bombs with 23 mL Teflon liners were used for the solvothermal reaction. In a typical synthesis, 10 mmol (5.4 g) of the precursor, $BaTi[OC_3H_7]_6$, was added to the Teflon liner of a digestion bomb under an inert atmosphere. A total of 10 mL of solvent was added to the precursor under flowing argon according to the water and isopropanol ratios in Table 1. In none of the solvents used did the precursor dissolve, but rather it formed a thick white suspension. The Teflon liner was tightly sealed inside the acid digestion bomb, and the mixture was heated in an oven at 220 °C for 18 h. The resulting white precipitate was collected by

centrifugation, washed with ethanol, and allowed to dry under ambient conditions. A white powder suitable for powder XRD and Raman measurements was produced with a typical yield of 1.93 g. Transmission electron microscope (TEM) images were taken on a JEOL 100CX instrument by using an accelerating voltage of 100 kV.

Raman Spectroscopy. Raman spectroscopy was performed in air by using a backscattering micro-Raman spectrometer with helium−neon laser (633 nm) excitation. A home-built thermoelec-tric heating stage was used for temperature-dependent measure-ments. Spectra were taken at temperatures ranging from room temperature to above 150 °C. The 300 cm^{-1} peak[35] was fit to a Lorentzian line shape on a sloping baseline, and from this fit, the scaled peak area and linewidth were determined.

Differential Scanning Calorimetry. Differential scanning cal-orimetry (DSC) was performed on a Perkin-Elmer Pyris 1 DSC. For each scan, 3−4 mg of sample was used. The heating profile consisted of two cycles of heating from 0 to 150 °C at a rate of 10 °C/min and then cooling from 150 to 0 °C at that same rate.

Thermodiffraction. X-ray diffraction data were obtained by using a Rigaku rotating anode together with a custom-built four-circle diffractometer. Graphite monochromated Cu Kβ radiation (1.39217 Å), together with a matched graphite analyzer, was used in Bragg−Brentano geometry. In this way, a well-defined powder diffraction profile was obtained for all reflections, allowing a detailed analysis of the profile changes associated with the paraelectric-to-ferroelectric phase transition. The intensities were normalized to the incident beam to eliminate drift over the data acquisition time. A home-built heating stage was used to reach temperatures up to 150 °C. X-ray patterns above 143 °C were collected to obtain a cubic reference for the expected increase in the peak widths with 2θ. Full pattern refinements were executed in the program Winprep[46] by using the profile parameters obtained from the cubic phase above 143 °C.

Synchrotron X-ray Diffraction. Synchrotron powder diffrac-tion data were collected in transmission mode at beamline 11-ID-B of the Advanced Photon Source, Argonne National Laboratory, by utilizing high-energy X-rays (∼90 kV) at room temperature. The use of high-energy X-rays enables measure-ments at longer wavevectors, $Q = 4\pi \sin(\theta/\lambda)$, which is important for the application of the PDF technique. Samples were loaded in Kapton tubes, and scattering data were collected on an image plate system (amorphous silicon detector from General Electric Healthcare) with sample-to-detector distances of 660 mm for Rietveld refinement data and 150 mm for PDF data. The raw data sets were processed to one-dimensional X-ray diffraction data by using the program FIT2D.[47] A bulk internal standard was used to calibrate the processed data, to supply an effective wavelength of $\lambda = 0.13648$ Å for refinements. Rietveld refinement of the synchrotron data was carried out in the XND program.[48] Lattice parameters, atomic positions, and atomic displacement parameters were refined. The PDF, $G(r) = 4\pi r[\rho(r) - \rho_0]$, was extracted from the processed scattering data as described by Chupas et al.[49] with a maximum momentum transfer of $Q = 24$ Å^{-1} by using the program PDFGETX2.[50] In this equation, $\rho(r)$ is the local atomic number density, ρ_0 is the average atomic number density, and r is the radial distance. Full structure profile refinements were carried out in the programs PDFfit2 and PDFgui.[51] The scale factor, lattice parameters,

(45) Niederberger, M.; Garnweitner, G.; Pinna, N.; Antonietti, M. *J. Am. Chem. Soc.* **2004**, *126*, 9120–9126.

(46) Stahl, K. *Winprep*; Lyngby, Denmark.

(47) Hammersley, A. P.; Svensson, S. O.; Hanfland, M.; Fitch, A. N.; Hausermann, D. *High Pressure Res.* **1996**, *14*, 235–248.

(48) Bèrar, J. F.; Garnier, P. *NIST Spec. Publ.* **1992**, *846*, 212.

(49) Chupas, P. J.; Qui, X.; Hanson, J. C.; Lee, P. L.; Grey, C. P.; Billinge, S. J. L. *J. Appl. Crystallogr.* **2003**, *36*, 1342–1347.

(50) Qiu, Y.; Wu, C. Q.; Nasu, K. *Phys. Rev. B* **2005**, *72*, 224105-1–224105-7.

(51) Farrow, C. L.; Thompson, J. W.; Billinge, S. J. L. *J. Appl. Crystallogr.* **2004**, *37*, 678.
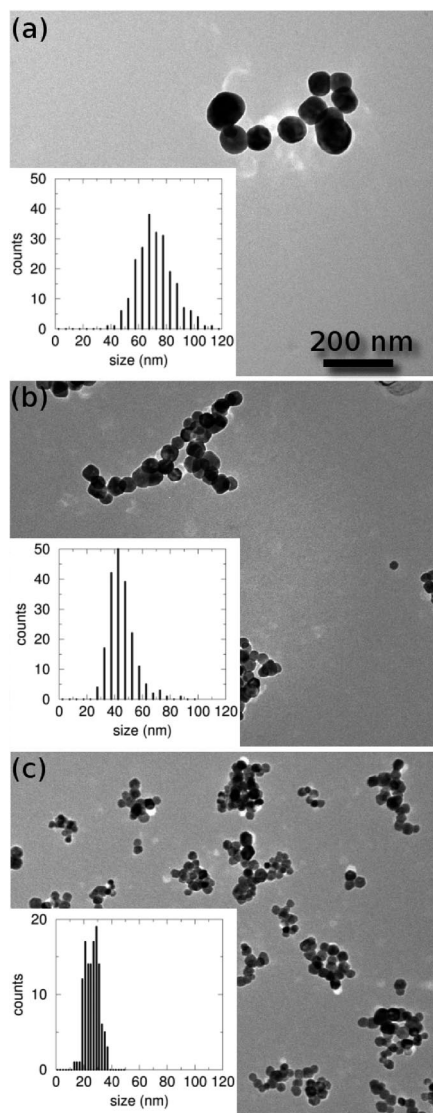
Figure 2. TEM images of BaTiO$_3$ nanoparticles. Histograms of individual particle sizes, shown as insets, correspond to (a) 70 ± 10 nm, (b) 45 ± 9 nm, and (c) 26 ± 5 nm. The 200 nm scale bar is common to all three micrographs.

atomic displacement parameters, and atomic positions as well as broadening from the sample and the instrument resolution were refined.

Results and Discussion

Preparation of BaTiO$_3$ Nanoparticles. We explored the effects of reaction conditions such as temperature, precursor concentration, solvent composition, and addition of surfactants in the preparation of BaTiO$_3$ nanoparticles. We found that the composition of the solvent played a critical role in determining the size of the particles, pure water producing the largest sizes and pure isopropanol producing the smallest. A TEM was used to determine the particle size and morphology, and typical images are shown in Figure 2, with histograms of the particle-size distributions displayed as insets. The particles were nearly spherical in shape with average sizes of 70, 45, and 26 nm. Table 1 gives the average particle size obtained with each solvent mixture as determined by TEM; the given error is plus

or minus one standard deviation. Scherrer analysis[52] of the laboratory XRD (111) peak at room temperature gave X-ray coherence lengths (grain sizes) of 33, 29, and 21 nm for the 70, 45 and 26 nm particles, respectively. The instrumental line width limits the determination of particle size to a maximum of 35 nm, preventing any conclusions about the single crystallinity (grain size) of the 70 nm particles. However, for the two smaller sizes, the individual particles are likely single crystals.

The final size of the particles is determined by the balance between particle nucleation and growth. In order to form BaTiO$_3$ from the alkoxide precursor, M−O−M bonds must be formed from M−OR species (M = Ti, Ba; R = −OC$_3$H$_7$). In the mixed solvent system, it is likely that several mechanisms are in competition with one another, determining the reaction pathway. In pure water, the pH of the solvent−precursor solution was 13, suggesting the partial hydrolysis of the precursor to Ba(OH)$_2$. This M−OH species can react with a second M−OH or with an M−OR to form the M−O−M bonds and water or isopropanol, respectively. M−O−M bonds might also form through a β-hydride elimination and the reaction of the metal hydride with an M−OR. An additional effect of the solvent composition is that the isopropyl group is a better capping group than the hydroxide because −OC$_3$H$_7$ is less reactive than −OH. Isopropoxy moieties on the surface of a particle passivate the surface, inhibiting particle growth and leading to smaller particle sizes.

Raman Spectroscopy. Tetragonal BaTiO$_3$ has 10 Raman-active modes. When splitting of transverse and longitudinal optical modes, as well as splitting due to differing polarizability in each unit cell direction is considered, 18 Raman-active phonons result.[53] Symmetry demands that cubic BaTiO$_3$ should be completely Raman-inactive. However, broad peaks centered at 260 and 530 cm^{-1} are still observed above the cubic-to-tetragonal phase-transition temperature.[34] The Raman activity of the cubic phase has been generally attributed in the literature to disorder of titanium in the nominally cubic phase.[53]

Figure 3 shows the Raman spectrum of (a) bulk, (b) 70 nm, (c) 45 nm, and (d) 26 nm BaTiO$_3$ over a range of temperatures between 25 and 150 °C. The assignments given to the Raman modes at the top of Figure 3 are those reported in the literature.[34] Below 200 cm^{-1}, we find some weak scattering in the nanoparticle samples due to a BaCO$_3$ impurity. As seen by others, the BaTiO$_3$ Raman spectra have the broad features characteristic of titanium disorder in the unit cell at all temperatures and at all sizes. In the bulk BaTiO$_3$ spectra in Figure 3a, the intensities of the E(LO + TO), B_1 peaks at ∼300 cm^{-1} and E(LO), A_1(LO) peaks at ∼715 cm^{-1} decrease rapidly as the temperature increases through the bulk T_C, an observation consistent with prior reports.[35] We interpret the disappearance of the 300 cm^{-1} peak as an indicator of the tetragonal phase and use two characteristics as an indication of the phase transition. The first is an increase in peak width at the phase-transition temperature similar to that reported by Hoshina et al.,[15] and the second is the loss of peak intensity with increasing temperature. These values are given in Figure 4a−d.

For all samples, the linewidth for the E(LO + TO), B_1 peak increases both with increasing temperature and with decreasing particle size. The much larger linewidths of the Raman peaks of the nanoparticles suggest that the tetragonality present is accompanied by a significantly decreased structural coherence.

(52) Cullity, B. D.; Stock, S. R. *Elements of X-ray Diffraction*, 3rd ed.; Prentice Hall: Upper Saddle River, NJ, 2001.
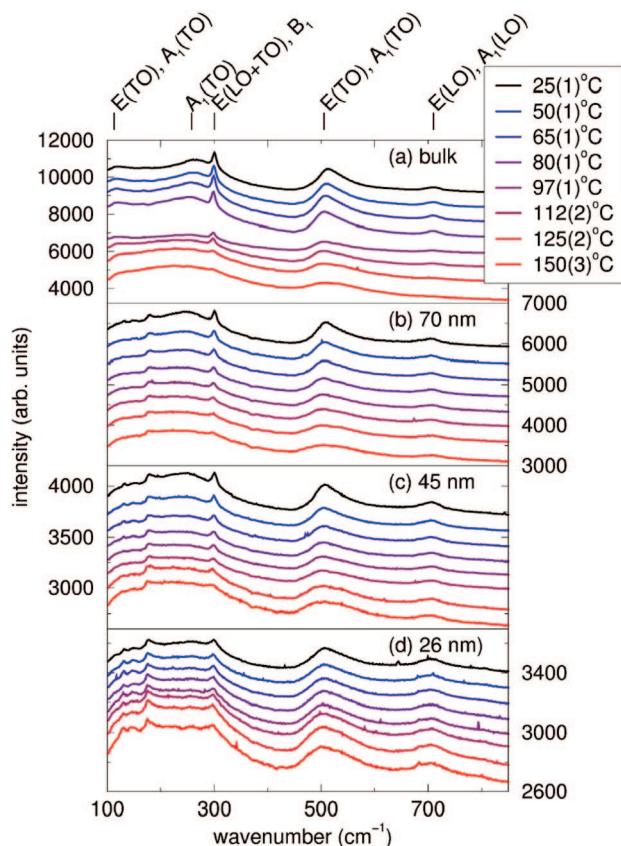(53) DiDomenico, M.; Wemple, S. H.; Porto, S. P. S. *Phys. Rev.* **1968**, *174*, 522–530.

Figure 3. Raman spectra at different temperatures for (a) bulk BaTiO₃, (b) 70 nm particles, (c) 45 nm particles, and (d) 26 nm particles. Temperatures increase from top to bottom in each panel. Temperatures are specified to be within a range of up to ±3 °C. The locations of Raman modes are indicated at the top of the figure. The features below 200 cm⁻¹ are due to a trace BaCO₃ impurity, and these are not found in the bulk sample.

It is interesting to note that bulk BaTiO₃ near the cubic-to-tetragonal phase transition displays a Raman linewidth that is similar to the line width displayed by the 26 nm particles at all temperatures.

The linewidth analysis is complemented by the analysis of scaled peak area. Figure 4 shows that near the expected phase-transition temperature of 130 °C, there is a sharp drop in the Raman intensity of the 300 cm⁻¹ peak for the bulk sample but a more gradual decrease in intensity over the entire temperature range for the 70 and 45 nm particles. In contrast, the peak area of the 26 nm particles in Figure 4d is nearly constant over the entire temperature range. These results indicate a phase transition that becomes increasingly diffuse in temperature as the particle size decreases.

The lack of a sharply defined phase transition in nanosized samples is also observed by using DSC. For bulk BaTiO₃, the DSC trace exhibits a peak near 130 °C, indicative of the phase transition. Similar features are not observed in the DSC of nanoparticle samples. Together with the Raman results, these findings support the idea that the phase transition is distributed over a wide range of temperatures in the nanoparticles, although it is sharply defined in the bulk material.

Thermodiffraction. The splitting of the X-ray diffraction peaks is well defined in terms of symmetry, allowing analysis of systematic changes for different (hkl) indices. Figure 5 shows diffraction data for 70 nm BaTiO₃ at room temperature and at 148 °C over a small 2θ range. In the high-symmetry cubic phase,
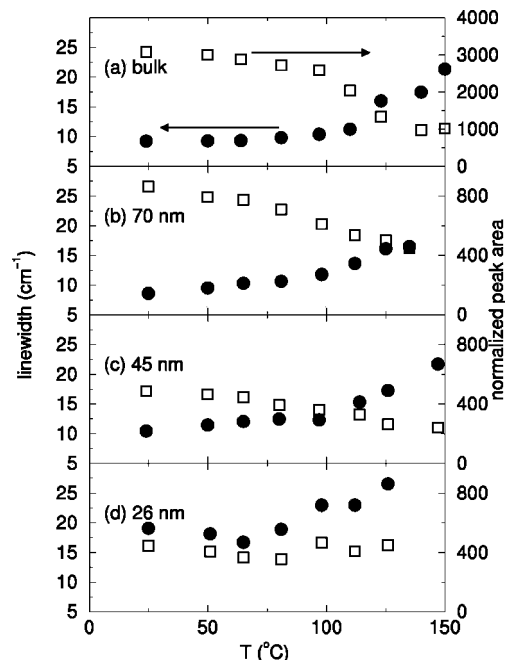

Figure 4. Results from fits to the Raman data. Filled circles show variation of the linewidth of the 300 cm⁻¹ Raman signal as a function of temperature. Open squares are intensities of the 300 cm⁻¹ Raman signal normalized to the intensity at 280 cm⁻¹. Displayed for (a) bulk powder, (b) 70 nm particles, (c) 45 nm particles, and (d) 26 nm particles.
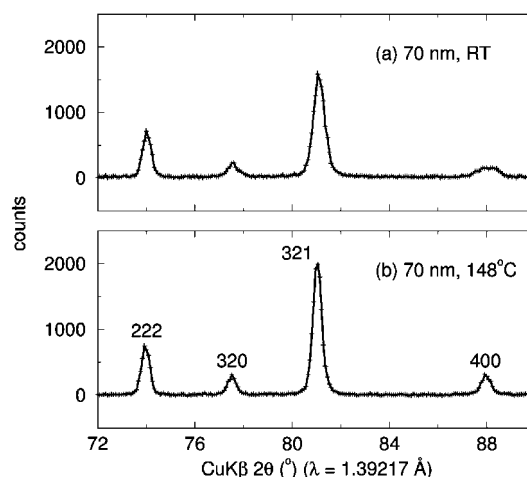

Figure 5. 70 nm BaTiO₃ particle laboratory XRD data shown over a small 2θ range. (a) Recorded at room temperature. (b) Recorded at 148 °C. Reflections have been labeled for the cubic phase in panel b. The (222) peak does not split in the tetragonal phase, and consequently, the peak width is constant with temperature. Peaks which are degenerate in the cubic phase but not in the tetragonal phase, for example cubic (400), widen and lose intensity upon cooling.

no reflections are split. In the tetragonal phase, (222) remains a single peak whereas the (400) reflection is divided into (400/ 040) and (004) peaks with an intensity ratio of 2:1. Because the c/a ratio is larger than 1, the (004) reflection shifts to a lower 2θ value, and the (400/040) reflection correspondingly shifts to a higher 2θ value. In spite of changes in symmetry, the cubic-to-tetragonal phase transition is usually not well resolved in diffraction studies of nanosized BaTiO₃ because of inherent line broadening due to small particle size.

In our study, the phase evolution of BaTiO₃ particles was determined by pattern matching to the laboratory X-ray dif-
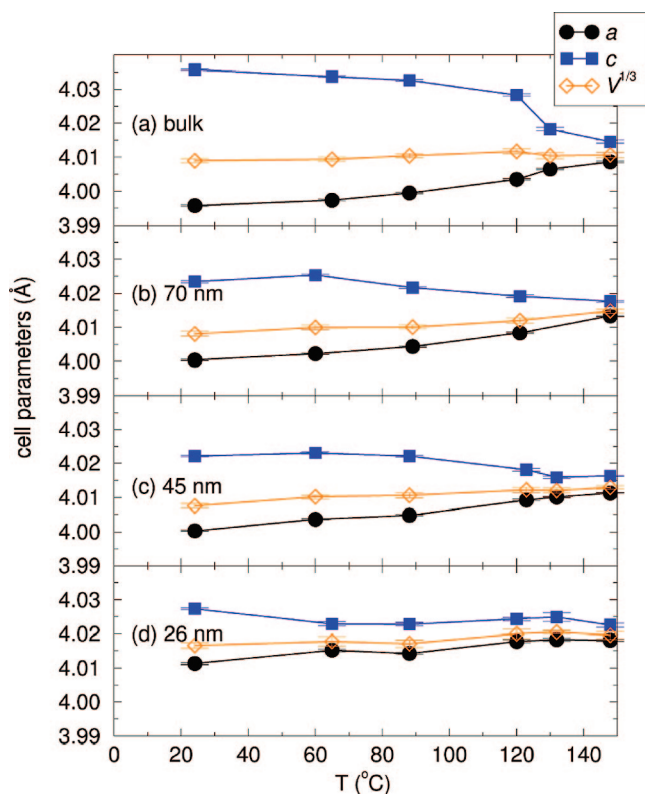
Figure 6. Change in a and c cell parameters and pseudocubic cell parameter for (a) bulk, (b) 70 nm particles, (c) 45 nm particles, and (d) 26 nm particles from pattern matching to laboratory diffraction data. Uncertainty in temperature for all data points is ± 2 °C.

fraction data. Patterns taken above T_C were matched to the cubic phase to determine the intrinsic peak profile resulting from particle size and instrumental effects. To investigate structural changes with temperature, all data sets were pattern-matched with a tetragonal unit cell, even above the phase transition, by using this fixed profile function.

Figure 6a–d shows the refined values of the length of the a and c cell parameters at each temperature for bulk, 70, 45, and 26 nm particles. The pseudocubic cell parameter (the cube root of the unit cell volume) is also shown. In Figure 6a, we see that for the bulk particles, there is at first a gradual change in a and c cell parameters as temperature increases. The rate of change becomes the greatest at the transition temperature, at which point the c/a ratio drops to its cubic-phase value of unity. This behavior is well known for the bulk material and has been explained as a second-order phase transition followed by a first-order phase transition.[3] In contrast to the behavior of the bulk material, the three sizes of particles studied here undergo a more gradual change in cell parameters, without a dramatic increase in slope at the phase transition temperature (Figure 6b–d).

At room temperature, the c/a ratio for the bulk sample was calculated to be 1.010, close to the value of 1.011 reported in the literature.[28] The ratio diminishes for decreasing particle size, with values of 1.0058(1), 1.0055(1), and 1.0040(2) for particle sizes of 70, 45, and 26 nm, respectively. For 26 nm particles, the deviation of c/a from unity is about 40% of that for the bulk tetragonal phase. Depressed c/a values have been modeled as a result of decreased polarization near the particle surface.[22] The picture of an increasingly broadened phase-transition behavior with decreasing particle size is consistent across the analysis of Raman spectra, DSC measurements, and XRD.

Table 2. Results of Rietveld Refinement of the Synchrotron X-ray Diffraction Data Collected at a Wavelength of $\lambda = 0.13648$ Å[a]

	70 nm	45 nm	26 nm
	4.0003(2)	4.0044(3)	4.0125(5)
c (Å)	4.0265(4)	4.0254(6)	4.030(1)
c/a	1.0065(10)	1.0054(3)	1.0044(4)
vol (Å^3)	64.43(1)	64.55(1)	64.88(2)
z(Ti)	0.518(1)	0.524(1)	0.534(1)
z(O1)	0.008(8)	0.004(10)	0.003(9)
z(O2)	0.490(5)	0.506(5)	0.508(5)
BaCO$_3$ mol%	3	6	11
R_w (%)	1.92	2.00	2.68

[a] A second BaCO$_3$ phase was also refined, and the mole fractions of the second phase are presented.
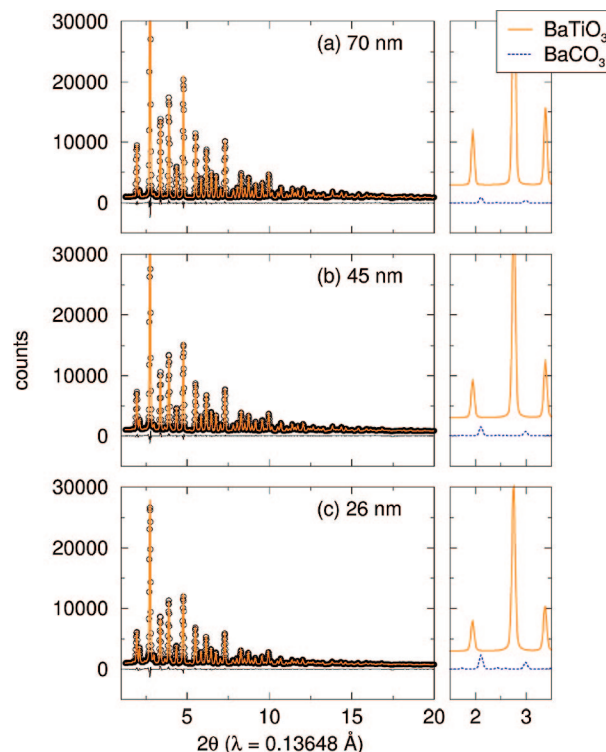

Figure 7. Rietveld fits of the synchrotron X-ray data for (a) 70 nm particles, (b) 45 nm particles, and (c) 26 nm particles. Data are shown as circles, and the solid orange lines are fits with two phases: BaTiO$_3$ and BaCO$_3$. Phase contributions from BaTiO$_3$ and from the BaCO$_3$ impurity are displayed across a small 2θ region at the right of each panel. In panels a and b, the most intense peak has been cut off in order to show all data sets at the same scale.

Synchrotron Rietveld and PDF Analysis. Rietveld refinement results of high-energy, long wavevector (Q) synchrotron X-ray diffraction for the three sizes of nanoparticles in this study are given in Table 2, and the corresponding fits are shown in Figure 7. The data have been fit with the $P4mm$ tetragonal model, as established from the pattern matching analysis. An orthorhombic BaCO$_3$ impurity phase was included in the refinements. The right panels in Figure 7 show the respective phase contributions to the fits from BaTiO$_3$ and BaCO$_3$. Table 2 includes results of a quantitative phase analysis from the refinement. Phase impurities of 11, 6, and 3 mol% for particle sizes of 26, 45, and 70 nm are determined, respectively, in agreement with the relative increase of BaCO$_3$ scattering in the Raman data of the smaller particles. We do not expect any influence of this separate phase on Raman and X-ray results.

Synchrotron Rietveld refinement results suggest several trends as particle sizes are reduced and are displayed graphically in
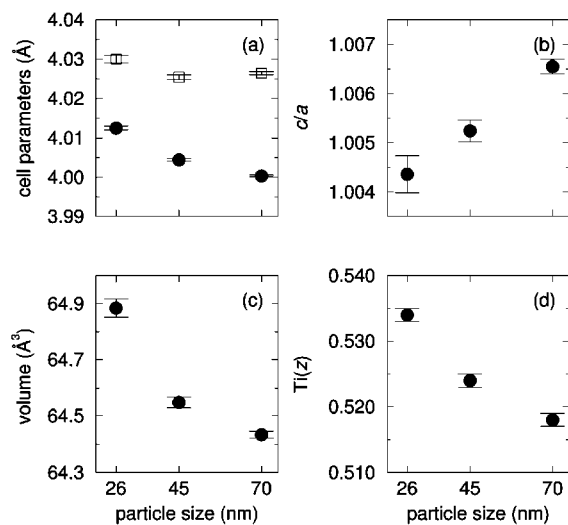
Figure 8. Rietveld refinement results for synchrotron data for the different particle sizes. (a) Cell parameters (*c* is the larger value), (b) *c/a* ratio, (c) cell volume, and (d) *z* position of titanium in the tetragonal *P4mm* phase.

Figure 8. For reference, previous neutron studies of the bulk material give a cell volume of 64.271(14), a *c/a* ratio of 1.011, and a *z*(Ti) position of 0.5224(6).[28] Lattice parameters are shown in Figure 8a, indicating larger *a* and *c* values for smaller particle sizes. In Figure 8b, the *c/a* ratio is shown. The *c/a* values decrease for smaller particle sizes: 1.0065(10), 1.0054(3), and 1.0044(4) for 70, 45, and 26 nm particles, respectively. Cell volume is presented in Figure 8c, increasing for the same series as 64.43(1), 64.55(1), and 64.88(2) Å³. These results are consistent with pattern matching results. The increase in unit cell volume is well established in the literature for many metal oxides[54–57] and has been observed in studies of small particles of BaTiO₃.[57] This is in contrast to metals such as gold, the cell parameters of which shrink as their size is diminished.[58] The most consistent explanation for such a volume expansion in small oxide particles is the effect of truncation on the attractive Madelung potential that holds the oxide lattice together.[59]

The *z*(Ti) positions from the Rietveld refinements are plotted in Figure 8d. Surprisingly, the titanium displacements increase with decreasing particle size, corresponding to 0.0725(1), 0.0966(2), and 0.1370(3) Å displacements in the unit cells of 70, 45, and 26 nm particles, respectively. This is surprising given that the system becomes more cubic with reduced size. This average structure result motivates us to look at the local structure.

Local structure analysis was carried out in the *P4mm* space group, with only the *z*(Ti) position refined. Our PDF analysis is based entirely on metal–metal distances (metal positions are reliable for X-ray scattering) and was not changed by including the refinement of O1 and O2 oxygen positions. We performed
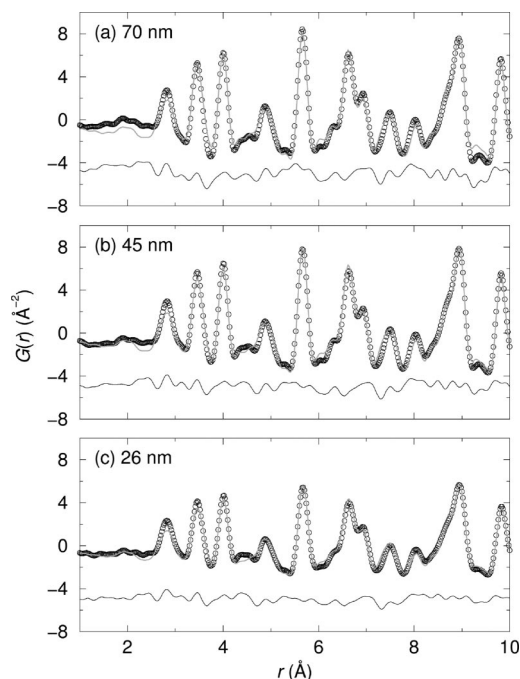
(54) Ayyub, P.; Palkar, V. R.; Chattopadhyay, S.; Multani, M. S. *Phys. Rev. B* **1995**, *51*, 6135–6138.

(55) Thapa, D.; Palkar, V. R.; Kurup, M. B.; Malik, S. K. *Mater. Lett.* **2004**, *58*, 2692–2694.

(56) Li, G.; Boerio-Goates, J.; Woodfield, B. F.; Li, L. *Appl. Phys. Lett.* **2004**, *85*, 2059–2061.

(57) Ishikawa, K.; Uemori, T. *Phys. Rev. B* **1999**, *60*, 11841–11845.

(58) Mays, C. W.; Vermaak, J. S.; Kuhlmann-Wilsdorf, D. *Surf. Sci.* **1968**, *12*, 134–140.

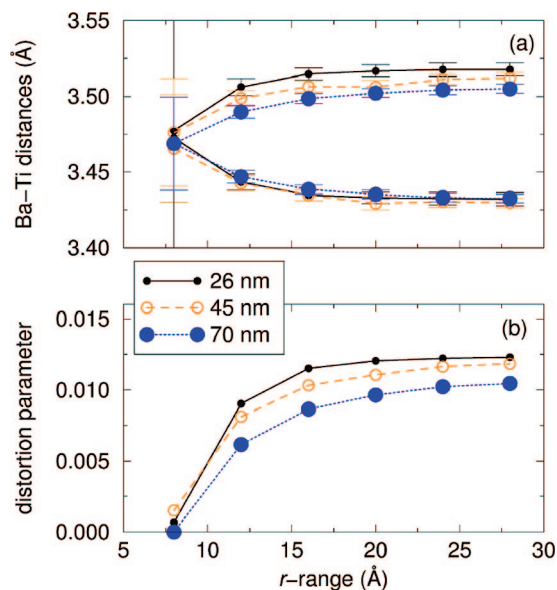(59) Perebienos, V.; Chan, S. -W.; Zhang, F. *Solid State Commun.* **2002**, *2002*, 295–297.

Figure 9. PDF fits of the total X-ray scattering for the different particles. Circles correspond to the experimental PDFs, and the fits are gray lines through the data. The difference curves are displayed in each panel and have been offset for clarity.

Table 3. Results of Real Space PDF Refinements over a 20 Å Range[a]

	26 nm	45 nm	70 nm
a (Å)	3.9972(5)	3.9961(5)	3.9926(4)
c (Å)	4.041(1)	4.029(1)	4.0294(8)
c/a	1.0109(4)	1.0082(4)	1.0092(3)
vol (Å³)	64.56(6)	64.34(4)	64.23(4)
z(Ti)	0.518(2)	0.516(2)	0.514(1)
z(O1)	0	0	0
z(O2)	0.5	0.5	0.5
U_{iso}(Ba)	0.00415(6)	0.00365(5)	0.00325(4)
U_{iso}(Ti)	0.0090(4)	0.0078(3)	0.0072(2)
U_{iso}(O1,O2)	0.0227(3)	0.0227(3)	0.0224(2)
R_{w} (%)	16.0	14.8	19.1

[a] A tetragonal *P4mm* model was employed, with fixed O1 and O2 positions. Refined parameters are given with error.

tetragonal model fits from 8 to 28 Å of real space, in 4 Å supplements. Figure 9 displays the first 10 of 20 Å fits to the experimental nanoparticle PDFs, *G*(*r*), in real space, and Table 3 presents the PDF results of the 20 Å refinements. The first atom–atom distance manifested in the BaTiO₃ PDF corresponds to Ti–O distances near 2 Å. Ba–O distances come next around 2.8 Å, followed by Ba–Ti distances at around 3.5 Å and the first Ba–Ba distances around 4 Å. Qualitatively, the intensity of atom–atom peaks decrease, and the widths increase with decreasing particle size.

In the *P4mm* space group, Ba–Ba distances are manifested in *a* and *c* cell parameters, and Ba–Ti distances depend on both the cell parameters and titanium off-centering. Consequently, cell parameters, the atom *z* positions, and the *c/a* ratio could all be used as metrics of departure from a centrosymmetric structure. Because *c/a* and *z*(Ti) are likely to be correlated in an analysis, this is perhaps best captured through examination of atom–atom distances. The off-centering of titanium creates four long and four short Ba–Ti distances within each unit cell.

Figure 10. PDF refinement results with varying *r* range. (a) Long and short Ba−Ti distances and (b) distortion parameter based on Ba−Ti distances as defined in the text.

We have parameterized the off-centering by using a distortion parameter, defined here as

$$\frac{(\text{Ba−Ti})_{\text{long}} - (\text{Ba−Ti})_{\text{short}}}{(\text{Ba−Ti})_{\text{long}} + (\text{Ba−Ti})_{\text{short}}}$$

The sensitivity of the PDF to short-range structure and local bond distance, rather than to long-range periodic structure, is the particular strength of the technique. This is traditionally most apparent when refinements are carried out over short *r* ranges. Figure 10a shows the extracted Ba−Ti distances, and Figure 10b shows the distortion parameter for the various *r* ranges used in this study and an unexpected result. The distortion is the largest in the high *r* range (relatively constant for $r \geq 16$ Å, the distance across about four unit cells) and is essentially absent in the low *r* region. The dependence on the *r* range is similar for all three particle sizes, suggesting that this is related to the type of modeling that we have used or the disorder present in the system and not to any size effect. This result perhaps supports the notion of decreased sensitivity of the local structure to the order−disorder picture first envisioned by Comes and Lambert.[31,32] Previous PDF studies of bulk $BaTiO_3$ phases above and below phase transitions have demonstrated small or negligible effects on the experimental $G(r)$.[60,61] A possible explanation is that the PDF is better poised to probe changes in displacive disorder than changes to the orientation of displacements, especially over low *r* ranges. Thus, the behavior of our fits at low *r* may suggest the length scale at which correlated order−disorder distortions in the particles may be captured. It should be emphasized that the low *r* behavior in this system is not completely understood and perhaps calls for higher-quality data (such as time-of-flight neutron PDF) or improved modeling.

Figure 11 shows the long and short Ba−Ti distances in panel a and the distortion parameter in panel b for the particle sizes,
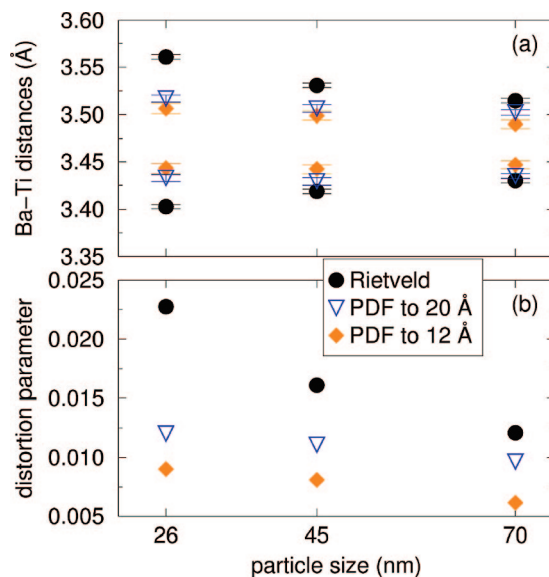
(60) Kwei, G. H.; Billinge, S. J. L.; Cheong, S. -W.; Saxton, J. G. *Ferroelectrics* **1995**, *164*, 57.
(61) Egami, T.; Billinge, S. J. L. *Underneath the Bragg Peaks: Structural Analysis of Complex Materials*; Pergamon Press Elsevier: Oxford, England, 2003.

Figure 11. (a) Long and short Ba−Ti distances and (b) distortion parameter, defined as [(Ba−Ti)$_{\text{long}}$ − (Ba−Ti)$_{\text{short}}$]/[(Ba−Ti)$_{\text{long}}$ + (Ba−Ti)$_{\text{short}}$]. Results from synchrotron Rietveld refinements as well as the PDF analysis for different *r* ranges are displayed.

as extracted from Rietveld, 12 Å PDF, and 20 Å PDF analyses. It is again displayed that measured distortion increases with the length scale of the probe used for analysis. This is a counter-intuitive result, as we expect atomic distortions to be manifested most strongly in the low *r* region of the PDF and become less and less apparent at high *r*.

Despite these questions, both Rietveld and PDF suggest that as particle size decreases, the unit cell becomes metrically more cubic, but the displacement of titanium is actually enhanced. These results are reconciled if we consider that for the smaller particles, the distortions from one unit cell to another become less correlated and lose their coherence, in much the same manner as what is seen when bulk samples are heated to near the phase-transition temperature. Two physical explanations for an increasing distortion at smaller particle sizes suggest themselves. The first supposes that the increase in cell volume in smaller particle sizes allows more space within the unit cell for titanium off-centering. The second presumes that the reduction in periodicity in the lattice of smaller particles diminishes the restoring Coulombic force on movable atoms.

Conclusion

We observe by using DSC and Raman spectroscopy that nanoparticulate $BaTiO_3$ undergoes a cubic-to-tetragonal phase transition over a wide temperature range, in contrast to the sharp transition found in the bulk material. Our XRD data show that the tetragonal metric is reduced from the bulk value with decreasing size, but that particles as small as 26 nm remain in the tetragonal phase until near the bulk transition temperature. By using a combination of Rietveld and PDF analysis of synchrotron X-ray diffraction data, we establish a trend of increasing distortion in Ba−Ti distances and titanium off-centering with decreasing particle size. We conclude that although the smaller particles have a greater distortion, a loss of coherence relative to the bulk material is responsible for decreased *c/a* values. Our results significantly contrast the accepted wisdom that $BaTiO_3$ becomes less distorted for smaller particle sizes.

JA0758436